Impact of structural heterogeneity on upscaled models for large-scale CO_2 migration and trapping in saline aquifers

Sarah E. Gasda[a,*], Halvor M. Nilsen[b], Helge K. Dahle[c]

[a] *Center for Integrated Petroleum Research, Uni Research, Allégaten 41, N-5020 Bergen, Norway*
[b] *Applied Mathematics, SINTEF ICT, Forskningsveien 1, Oslo, Norway*
[c] *Department of Mathematics, University of Bergen, Allégaten 41, N-5020 Bergen, Norway*

Abstract

Structural heterogeneity of the caprock surface influences both migration patterns and trapping efficiency for CO_2 injected in open saline aquifers. Understanding these mechanisms relies on appropriate modeling tools to simulate CO_2 flow over hundreds of square kilometers and several hundred years during the postinjection period. Vertical equilibrium (VE) models are well suited for this purpose. However, topographical heterogeneity below the scale of model resolution requires upscaling, for example by using traditional flow-based homogenization techniques. This can significantly simplify the geologic model and reduce computational effort while still capturing the relevant physical processes.

In this paper, we identify key structural parameters, such as dominant amplitude and wavelength of the traps, that determine the form of the upscaled constitutive functions. We also compare the strength of these geologic controls on CO_2 migration and trapping to other mechanisms such as capillarity. This allows for a better understanding of the dominant physical processes and their impact on storage security. It also provides intuition on which upscaling approach is best suited for the system of interest.

We apply these concepts to realistic structurally heterogeneous surfaces that have been developed using different geologic depositional models. We show that while amplitude is important for determining the amount of CO_2 trapped, the spacing between the traps, distribution of spillpoint locations, large-scale formation dip angle affect the shape of the

*Corresponding author
Email address: sarah.gasda@uni.no (Sarah E. Gasda)

Preprint submitted to Adv. Water Resources *April 26, 2013*

function and thus the dynamics of plume migration. We also show for these cases that the topography characterized by shorter wavelength features is better suited for upscaling, while the longer wavelength surface can be sufficiently resolved. These results can inform the type of geological characterization that is required to build the most reliable upscaled models for large-scale CO_2 migration.

Keywords:
geological CO_2 storage, vertical equilibrium models, structural trapping, rough caprock, upscaling, geologic characterization, storage security

1. Introduction

Geological CO_2 sequestration in saline aquifers has the potential to store large volumes of anthropogenic CO_2 emissions and mitigate impacts of climate change [1]. The storage capacity of these aquifers depends primarily on structural, residual and solubility trapping acting to stabilize the CO_2 plume in the first 1000 years after injection has ceased [2]. The relative efficiency of these trapping mechanisms will be determined by geologic and fluid properties [3, 4]. Not only do these parameters affect capacity of a given formation for CO_2, but they also impact the long-term risk of leakage out of the formation. Understanding the impact of these mechanisms on CO_2 migration and trapping in open aquifers is an important goal of the CO_2 storage community.

Numerical simulation is an important component for understanding fundamental processes occurring in a CO_2 storage site as well as for estimating storage capacity, quantifying risk and managing storage operations. When applying numerical models to CO_2 migration and trapping, it is important that the scale of the model matches the scale of the processes to be simulated [5]. However, CO_2 injection involves large plume footprints that can extend several kilometers in lateral extent [6] and can potentially migrate up to 100 kilometers away from the injection well over 100s of years in open dipping aquifers [7]. Meanwhile, trapping mechanisms such as dissolution by convective mixing [8] and structural trapping in sub-seismic scale features [9] may occur at the scale of centimeters and meters. These large discrepancy in temporal and spatial scales need to be modeled simultaneously and presents a particular challenge for effective and reliable simulation of long-term evolution of the CO_2 plume.

Vertical equilibrium (VE) models have emerged in recent years as an alternative to full-physics models for simulating CO_2 injection and migration [5, 10, 11, 12, 13]. These reduced dimension models are effective at capturing the large-scale plume dynamics while coupling in subscale phenomena such as capillary effects [14] and enhanced dissolution by convective mixing [15]. In a recent paper [16], we have explored the utility of flow-based upscaling to capture subscale caprock topography on plume migration and trapping. We showed that upscaled permeability and relative permeability constitutive functions could be derived through analytical or numerical upscaling that simulate the reduced plume speed and enhanced trapping for relatively idealized systems.

One important aspect of these upscaled constitutive functions is that the shape of the function could be dependent on the type of surface being upscaled. For instance, a sinusoidal surface produces an effective relative permeability that more quickly approaches the function for a flat caprock surface (with no roughness) than a square-wave type of functions. However, these are idealized structures at the limits of real caprocks, and it was not clear how these functions would change for more realistic geological surfaces. In this paper, we explore the impact of different geologic controls on the form of the relative permeability functions. In addition, we develop a set of dimensionless groupings to compare the strength of surface roughness effect compared to the height of capillary fringe, which is another relevant physical phenomenon in CO_2 storage. Finally, we apply these concepts to simulate large-scale plume migration and trapping along realistic geological surfaces.

The results of this paper increase our understanding of which topographical parameters have the most impact on upscaled functions, as well as how best to apply upscaling approaches to different geological settings. If complex geology can be simplified, then computational efficiency increases significantly. Faster simulation allows for easier exploration of the parameter space and ultimately a better understanding of the impact of geological uncertainty on CO_2 migration.

2. Model description

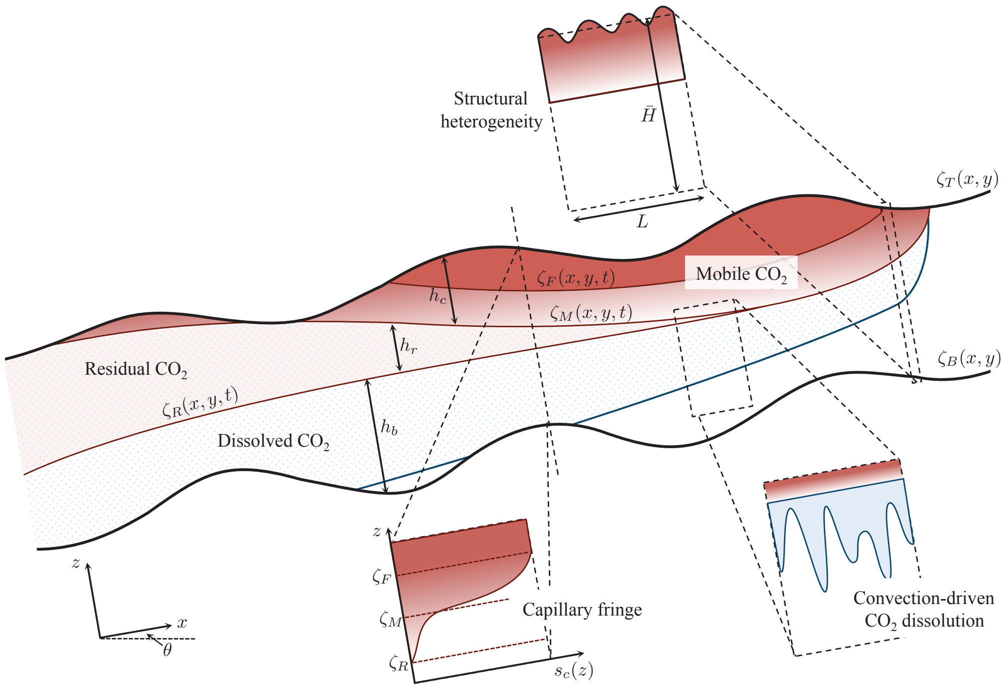

Figure 1: VE model CO_2 injection and migration with heights of brine, mobile CO_2, with associated capillary fringe, residually trapped CO_2, and region with dissolved CO_2. Insets show subscale processes that are implemented into the VE model used in this study, including structural heterogeneity, a capillary fringe, and convectively-driven CO_2 dissolution. The aquifer may be tilted at a large-scale dip angle θ relative to the horizontal, which may vary in space.

The VE model is employed for CO_2 injection into a deep saline aquifer. The model assumes a two-phase two-component system consisting of a CO_2-rich phase (subscript c) and a brine-rich phase (subscript b). The phases are slightly miscible such that CO_2 can dissolve into the brine phase and water can dissolve in the CO_2 phase. CO_2 migrates according to viscous and gravity-dominated forces, while CO_2 trapping occurs in the present model by structural, residual and solubility mechanisms. Mineral reactions with the host rock have been neglected.

Inherent in the VE model is the assumption that the fluids are segregated vertically so that capillary and gravity forces are balanced. This means that vertical equilibrium exists with respect to pressure, and vertical flow can be neglected. As a result, the vertical space bound by the top and bottom impermeable surfaces, $\zeta_T(x,y)$ and $\zeta_B(x,y)$, respectively, can be subdivided into macropscopic regions bounded by macroscopic interfaces. An example of this vertical structure is depicted in Figure 1. The topmost region is bound below by a dynamic interface $\zeta_M(x,y,t)$ and is created during the drainage process as CO_2 displaces brine. This region contains mobile CO_2 in a fully-drained zone and two-phase CO_2 and brine in a capillary transition zone, which are separated by an interface $\zeta_F(x,y,t)$ above which the CO_2 is at the endpoint saturation with residual brine. When flow reverses and ζ_M recedes, brine reimbibes the porespace and traps residual CO_2 in a region that is bound above by the ζ_M interface and below by another dynamic interface $\zeta_R(x,y,t)$. The lowest region of fluid is the undrained brine region bound above by ζ_R and below by the aquifer bottom at ζ_B. The structure is fixed such that $\zeta_B \leq \zeta_R \leq \zeta_M \leq \zeta_F \leq \zeta_T$

The consequence of capillary-gravity equilibrium is that a well-defined vertical structure in saturation is known. In the simplest case where capillary forces are small, the transition zone can be neglected ($\zeta_F = \zeta_M$) and we obtain the classical sharp-interface model. When capillary forces are strong, the saturation distribution in the relatively large fringe can be obtained from the local capillary pressure curve for the medium. This allows the three-dimensional equations to be integrated over the vertical dimension (perpendicular to the predominant flow direction), resulting in the VE model. The derivation can be performed under different further simplifications, such as a sharp interface or without solubility trapping. See [5, 17] for a full derivation.

2.1. Vertical equilibrium model

Integration of the fine-scale 3D equations leads to a mass conservation equation for the quantity M^α, which is the mass per unit area of component $\alpha = c, b$ summed vertically over the CO_2 and brine fluid phases,

$$\frac{\partial M^\alpha}{\partial t} + \nabla_\parallel \cdot \mathbf{F}_\parallel^\alpha = Q^\alpha, \quad \alpha = c, b, \tag{1}$$

where $\mathbf{F}_\parallel^\alpha$ is the depth-integrated lateral mass flux of component α across all phases, and Q^α is the source/sink term of component mass per area. The lateral direction is assumed to be parallel to the large-scale dip angle of the aquifer, $\theta(x, y)$, which may vary in space. For convenience, we will omit the $(\cdot)_{\parallel}$ notation from this point forward.

The integrated mass fluxes, defined in [15], lead to component fluxes which can be divided into the three macroscopic regions of the aquifer. For example, $\mathbf{F}^c$ is composed of the sum of CO_2 mass flux with the CO_2 phase ($\mathbf{F}_c^c$) and as a dissolved component with the brine phase ($\mathbf{F}_b^c$),

$$\mathbf{F}_c^c = \int_{\zeta_M}^{\zeta_T} \mathbf{u}_c \rho_c m_c^c \, \mathrm{d}z, \tag{2}$$

$$\mathbf{F}_b^c = \int_{\zeta_R}^{\zeta_M} \mathbf{u}_b \rho_b^{mix} m_b^c \, \mathrm{d}z + \int_{\zeta_B}^{\zeta_R} \mathbf{u}_b \omega \rho_b^{mix} m_b^c \, \mathrm{d}z. \tag{3}$$

Here, ρ_c and ρ_b^{mix} are the density of the CO_2 phase and brine phase with dissolved CO_2, respectively, while the parallel components of fine-scale phase fluxes, $\mathbf{u}_\beta$, are given by Darcy's law [18, 15]. Dispersion of dissolved CO_2 is neglected due to the very large spatial scales and relative homogeneity of the system.

Mass flux in the CO_2 phase depends on the water solubility as a mass fraction, m_c^b, where $m_c^c + m_c^b = 1$. The flux of dissolved CO_2 is a function of the occurrence of dissolved CO_2 within the residual CO_2 region and below ζ_R. The former is governed by equilibrium partitioning given a solubility limit, m_b^c, while the latter is parameterized by a dynamic term, ω, that is a normalized mass fraction parameter, ω. More details about upscaled CO_2 dissolution can be found in [15].

The mass conservation equation is accompanied by a transport equation for dissolved CO_2,

$$\frac{\partial M_b^c}{\partial t} + \nabla \cdot \mathbf{F}_b^c = C_{\mathrm{diss}} \left(\omega, \zeta_R\right), \tag{4}$$

where M_b^c is the mass per area of dissolved CO_2 in the brine phase and C_{diss} is the upscaled dissolution rate with units of mass per area per time [15]. Additionally, there is an incompressible conservation equation for the CO_2 fluid phase,

$$H \frac{\partial \left(\Phi S_c\right)}{\partial t} + \nabla \cdot \mathbf{U}_c = Q_c, \tag{5}$$

where Φ, S_c and U_c are the depth-averaged porosity, CO_2 saturation, and CO_2 phase flux, respectively, as defined in [16], and Q_c is the volumetric source/sink of the CO_2 phase.

The system of equations (1), (4), and (5), consisting of the primary coarse-scale variables P, S_c and M_b^c, can be solved using an IMPES-type strategy whereby the upscaled pressure variable P is solved implicitly under the assumption of an incompressible system, followed by an explicit solve for S_c and M_b^c. A pressure equation is formed by summing (1) and (4) over the phases. The summed equation results in an additional term that accounts for the volume change due to CO_2 dissolution, see [15, 10] for more details. For the transport equations, we consider a splitting type approach, evolving S_c (Equation (5)), the dissolved CO_2 M_b^c (Equation (4)), and ζ_R (by mass balance) in an iterative manner. The spatial domain is discretized and solved numerically using a standard finite-difference approximation.

2.2. Horizontal upscaling

In certain situations, the structural heterogeneity of the caprock may be too fine to be resolved and an upscaled representation of the surface is desired. An additional horizontal averaging of the VE equations presented above can be performed either by analytical or numerical techniques. If the surface fluctuations are periodic within a characteristic length scale L, such that L is much smaller than the scale of the domain, then we can apply steady-state flow-based homogenization techniques that have been traditionally used to upscale permeability and relative permeability of heterogeneous media [19, 20].

The concept of spatial heterogeneity in permeability is applicable here because fluctuations in aquifer thickness due to caprock roughness leads to heterogeneity in transmissibility, which is the effective permeability to horizontal flow. In addition, if the physics of the system is such that CO_2 forms a layer at the top of the aquifer, as discussed in Section 2, the depth-integrated relative permeability will be horizontally heterogeneous as well, even if the CO_2-brine interface is flat. This heterogeneity will exist despite having a homogeneous porous medium. Horizontal upscaling will result in smoother VE equations, where the effects due to small scale features are transferred to the relative permeability functions. This is in analogy of single phase upscaling where the upscaled equations have a smoother permeability

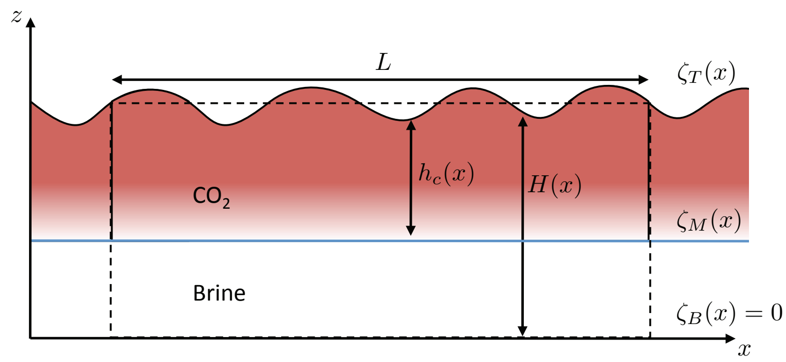

Figure 2: Caprock roughness at the horizontal fine-scale having spatially varying thickness $H(x)$ and CO_2 thickness $h_c(x)$ within the averaging length L. The system has a flat bottom $\zeta_B = 0$ and flat CO_2-brine interface. Adapted from [16].

than the fine-scale ones.

The details of the horizontal upscaling can be found in [16]. The objective of upscaling is to replace the varying top boundary $\zeta_T(x, y)$ with a flat surface over the two-dimensional averaging area with lateral length scale L^2. This results in an aquifer height that is constant and equal to the average of the thickness at the horizontal fine scale over the averaging length. In one spatial dimension this becomes,

$$\bar{H} = \frac{1}{L} \int_0^L \left[\zeta_T(x) - \zeta_B(x) \right] \, \mathrm{d}x. \tag{6}$$

The basic approach is to posit a homogeneous equation at the horizontal coarse scale composed of horizontally averaged quantities. We demonstrate this concept for one-dimensional flow of a single-phase equivalent of the depth-integrated phase flux U_α. Assuming steady-state flow over the averaging length then the fine-scale single-phase flow equation can be integrated and set equal to the homogeneous equation,

$$U_x = -\frac{\bar{H}\bar{K}_x}{\mu} \frac{\Delta p}{L}, \tag{7}$$

where Δp is the pressure gradient, and μ is the viscosity. Horizontally upscaled variables, such as $\bar{K}_x$, are indicated with an overbar.

For effective relative permeability $\bar{K}_\beta$, additional assumptions are required regarding the saturation at the horizontal fine-scale. Our approach is based on the capillary equilibrium assumption [20, 21] that is adapted to the VE rough caprock system and becomes an assumption on the CO_2-brine interface. For small pressure gradients and a horizontal averaging length much smaller than the domain, the CO_2-brine interface is essentially flat. This means that depth-averaged CO_2 phase saturation S_c can be fixed within the averaging window during the upscaling process. Then in a similar manner shown in Equation (7), the two-phase steady-state flow equation is compared with the corresponding homogeneous equation,

$$U_{\beta x} = -\frac{\bar{H}\bar{K}_x\bar{K}_{\beta x}}{\mu_\beta}\frac{\Delta p_\beta}{L}. \tag{8}$$

The homogeneous equations Equations (7)–(8) can be solved for $\bar{K}_x$ and $\bar{K}_{\beta x}$ if a fixed pressure gradient is applied and the steady-state flux is known. For one-dimensional cross-sections and simple two-dimensional surfaces, analytical expressions for the upscaled constitutive functions can be derived [16]. However, in general, numerical homogenization is necessary. To do this, steady-state flow simulations are performed by resolving the horizontal structure with the VE model described in Section 2.1. Periodic pressure boundary conditions are applied with a small pressure gradient in the horizontal direction. For asymmetric surfaces, the simulation must be performed in two dimensions to determine the diagonal and off-diagonal components.

For relative permeability calculations, the CO_2 is stationary with a vertical saturation distribution fixed according to the local capillary pressure equilibrium. We point out that if flow is faster due to a larger pressure gradient or the caprock surface is tilted, the stationary states for CO_2 saturation in the relative permeability calculations are not trivial and have to be found numerically. The details of the upscaling procedure are described in [16].

3. Characterization of upscaled constitutive functions

In this section we discuss the main characteristics which determine properties of the horizontally upscaled relative permeability functions discussed in Section 2.2. To identify these characteristics, we investigate a set of simplified or idealized caprock surfaces. An important consideration is that these parameters can be calculated for a given storage system given the available data from fine-scale geological models. These parameters can also be estimated for systems where a fine-scale model is not available.

We propose three sets of geologic parameters to be investigated. The first relates the characteristic width of the structural traps to the distance between each trap. The second relates the dominant wavelength of the structures, wide and shallow versus narrow and steep, and their amplitude, large versus small trapping volumes, to the effect of gravity due to aquifer tilt. The third takes into account surface effects, in particular the asymmetry of the surface and two-dimensional variation in spillpoint depths. The first two analyses can be performed on a one-dimensional surface, where the caprock is represented by a line, while the last must be solved numerically on a two-dimensional surface. We then compare the upscaled curves to the CO_2 relative permeability curve for a flat tilted surface (representing a locally smooth caprock), which is a linear function between zero and unity. This surface is referred to as a “flat” caprock from this point forward.

All numerical experiments were performed using a sharp-interface assumption with zero brine saturation under VE conditions. It should be noted that the VE assumption is valid for rough surfaces as long as the amplitude is much smaller than the wavelength.

3.1. Trapping volume and roughness

We have seen that the shape of the CO_2 relative permeability curve in previous work [16] is clearly a function of the volume of CO_2 that can be structurally trapped, called *structural residual saturation* because CO_2 must exceed a certain thickness before flow can occur in the upscaled sense. The potential trapping volume can be estimated from the amplitude of the structural features or from other simple trapping analyses [9]. Here, we refer to the amplitude ratio a as the amplitude scaled by the aquifer thickness,

$$a = \frac{A}{\bar{H}}. \tag{9}$$

Also, we have observed previously that different structures give varying degrees of roughness and impact the overall shape of the relative permeability function even when the trapping capacity is the same. A rougher surface means that CO_2 flow is slower and requires a greater plume thickness before the impact of the roughness becomes negligible, in which case CO_2 migration becomes similar to flow along a smoother caprock with only buoyancy due to large-scale dip as the dominant flow mechanism.

We take the specific example of an oscillating square wave, which was found to be the roughest surface compared to other structures for the same amplitude ratio [16]. Because the system is one-dimensional, the permeability and relative permeability can be derived by taking the harmonic average of the fine-scale quantities across the horizontal dimension, as described in [16]. The analytical permeabilities for a square and rectangular topographies are given in Table 1. The harmonic average is independent of wavelength, which is due to the single wave structure, but the amplitude ratio and other structural parameters impact the formula. For the rectangular wave, two relevant parameters are the length scales l_1 and l_2 that are associated with the distance between the structures and their width, respectively. The general case is a rectangle, such that $l_1 \neq l_2$. We can compute the ratio of these lengths as $f_r = l_1 / (l_1 + l_2)$, and compare different ratios for a given trapped volume to determine the impact of f_r on surface roughness. Given f_r, we can then derive the resulting formula for the rectangle, also in Table 1, which reduces to a square for $f_r = 0.5$.

The shape of the rectangle curves for different values of f_r, shown in Figure 3, varies between two limits. The limit when $f_r \to 0$ results in a linear function from $\bar{S} = a$ to unity. This case consists of structures that extend over the entire surface with an infinitesimally small distance separating them, which happens to correspond to the accretion layer model (AM) derived in [16]. The upper limit when $f_r \to 1$ results in a relative permeability that jumps from zero to the flat caprock curve at $\bar{S} = a$. This phenomenon occurs because, as the traps approach an infinitely small width of some volume, the surface essentially becomes identical to the reference flat caprock but with periodic instantaneous sinks. Thus, once the infinitely thin traps are filled, the relative permeability jumps from zero (no flow) to the reference flat surface curve (flow) because the traps do not affect flow once they are filled.

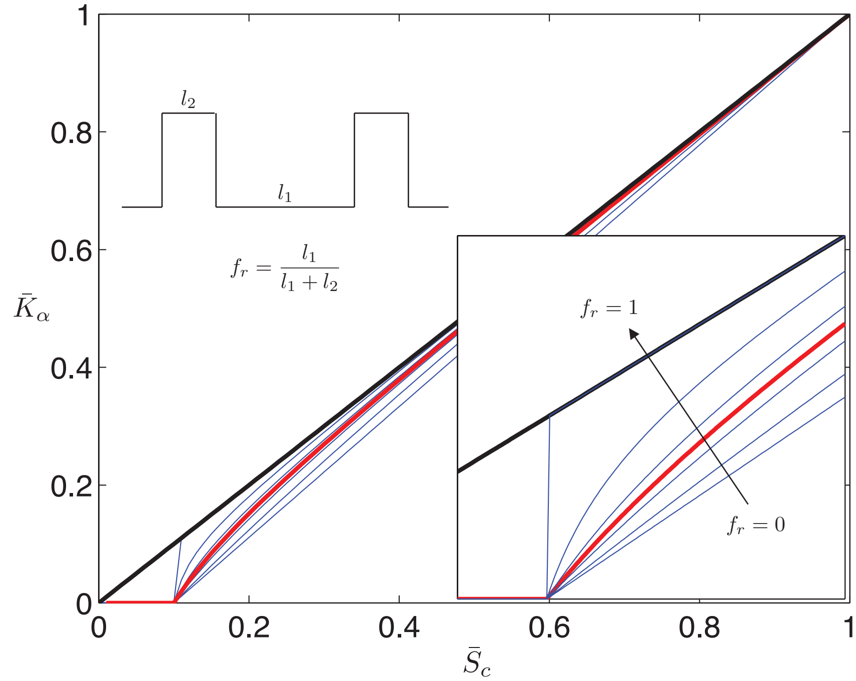

Figure 3: Upscaled CO_2 relative permeability curves for the rectangle surfaces for different values of roughness ratio f_r. The black line is the reference case–a linear relative permeability curve for a flat caprock– and the red is the square case with $f_r = 0.5$.

Table 1: Summary of effective permeability and relative permeability functions for different functional forms of caprock topography, where $\hat{h}_b = \bar{h}_b/\bar{H}$ and $\hat{h}_b \leq a$).

Topography	$\bar{K}$	$\bar{K}_b$	$\bar{K}_c$
flat	K	$k_b^0 \hat{h}_b$	$k_c^r \left(1 - \hat{h}_b\right)$
square	$K\left(1 - a^2\right)$	$k_b^0 \hat{h}_b$	$k_c^r \frac{\left(1 - \hat{h}_b\right)^2 - a^2}{\left(1 - \hat{h}_b\right)\left(1 - a^2\right)}$
rectangle	$K\left(\frac{f_r}{(1-a)+a/f_r} + \frac{1-f_r}{1-a}\right)^{-1}$	$k_b^0 \hat{h}_b$	$k_c^r \frac{\frac{f_r}{(1-a)+a/f_r} + \frac{1-f_r}{1-a}}{\frac{f_r}{(1-\hat{h}_b-a)+a/f_r} + \frac{1-f_r}{1-\hat{h}_b-a}}$

3.2. Effect of caprock tilt and wavelength

In the one-dimensional examples of sinusoidal waves studied in [16], the large-scale dip of the surface was assumed to be nearly horizontal. This simplification implies several things. First, the trapped volume of a horizontal surface is maximized for a given amplitude compared with the tilted surface. This occurs because the spillpoints are raised relative to the horizontal, allowing CO_2 to flow and thus reducing trapping capacity. Secondly, the upscaled relative permeability is independent of wavelength, λ, when the surface has zero dip angle. Additionally, there is a sharp transition in the CO_2 flow characteristics from the non-flowing to the flowing case, meaning that once CO_2 thickness exceeds the residual saturation the flowing CO_2 very quickly becomes flow along a smooth flat surface with only a small additional increase in CO_2 saturation.

We investigate the impact of large-scale tilt of the caprock, measured as the angle θ from the horizontal, by varying the tilt for a given sinusoidal amplitude and wavelength. Figure 5 shows that as θ increases, the residual saturation decreases, which is as expected. An additional striking qualitative change is a smoother transition from non-flowing to flowing regime with increasing θ. This result can be attributed to the extent of CO_2 flow along the "dry region," which is defined as the portion of the caprock under which no CO_2 accumulates or is trapped. At the limit when $\theta = 0$, the dry region is very small and therefore does not impact the flow once the residual saturation is exceeded. However, with a tilted surface, the dry region is larger and grows in size with increasing tilt. This means that CO_2 must flow along the dry region, which causes more resistance than the horizontal case. The size of the dry region increases with increasing wavelength and decreasing amplitude, all else being equal.

3.3. Two-dimensional surface effects

Above, we saw that increasing the tilt of the caprock surface in one-dimensional can introduce a smoother transition from the non-flowing to the flowing regime. A similar phenomena can occur due to varying depths of local minima (spillpoints) within the two-dimensional averaging window, as shown schematically in Figure 4. In the general case, CO_2

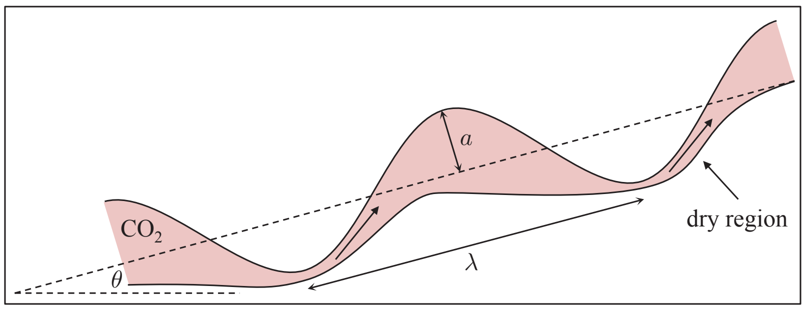

(a) sloping caprock

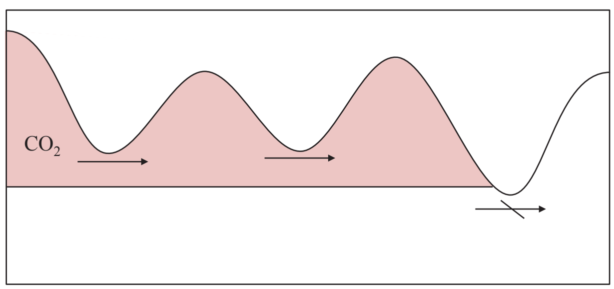

(b) spillpoint variation

Figure 4: Schematic of test cases for studying the tilt and surface impacts on CO_2 relative permeability. Top shows a 1D sloping sinusoidal caprock, with dry regions that contribute to surface roughness. Bottom shows a caprock with varying spillpoint depths that impact CO_2 flow. Here, a 1D cross-section of the generalized 2D surface is shown for ease of presentation.

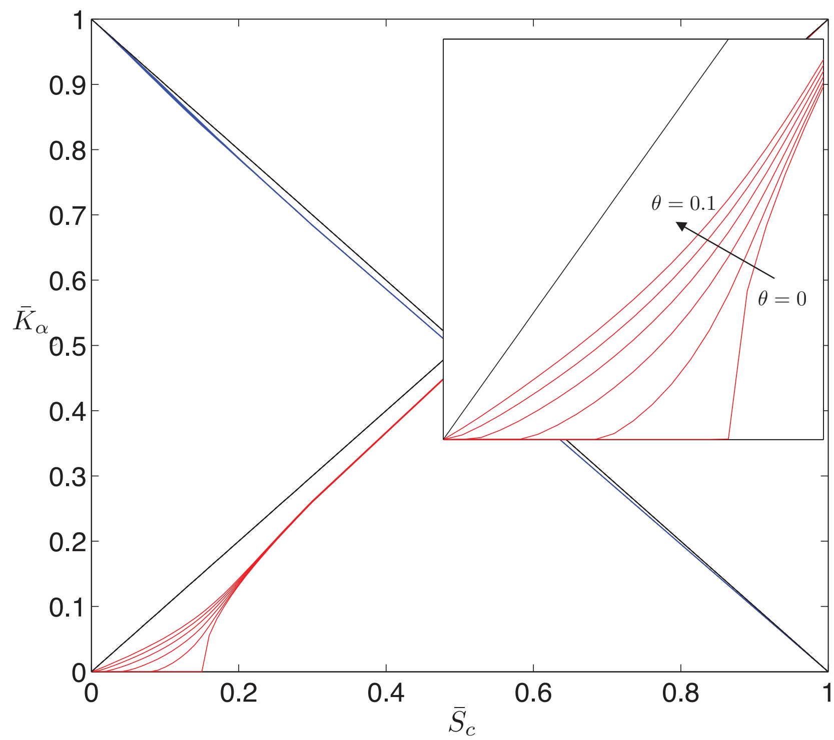

Figure 5: The upscaled relative permeability for CO_2 and brine for sinusoidal oscillation of the top surface with amplitude $A = 1.5$ meter ($a = 0.015$). The wavelength (λ) of the oscillation is 100 meter. The main figure shows the relative permeability for CO_2 (red) and water (blue). The different lines correspond to different angel of tilt θ of the reservoir. The inlet figure is a close up of the CO_2 relative permeability near zero.

will exceed only the shallowest spillpoint first, initiating flow along only a small portion of the surface. As CO_2 thickness increases, the flowing surface gradually increases until the deepest spillpoint is exceeded. This impact can occur even for a horizontal surface ($\theta = 0$), however it is solely a two-dimensional phenomenon since in the one-dimensional case CO_2 cannot flow until exceeding the deepest spillpoint.

Two scenarios were tested, one with constant and the other with varying spillpoint depth, as shown in Figure 6. The upscaled relative permeability curves show that the varying case leads to lower structural residual CO_2 saturation as flow is initiated earlier along the shallowest spillpoint compared to the constant case. We see that both the constant and varying case lead to anisotropic relative permeability tensors due to asymmetry of the surfaces, which leads to different flow characteristics in each dimension even in the constant case. The varying spillpoint depths can be an additional source of anisotropy. A perfectly symmetric surface (see [16]) will reduce to scalar relative permeability functions. And finally, we observe a smoother transition from non-flowing to fully flowing CO_2 in the varying case (for flow in the x direction), which implies a gradual increase in CO_2 relative permeability from the point of flow initiation until meeting the sharper curve for the constant case.

4. Application to realistic caprock surfaces

The insights obtained from the analysis in Section 3 can aid in characterizing the topography of more realistic caprock surfaces. This involves applying the numerical homogenization techniques described previously to upscale permeability and relative permeability functions. Additionally, flow simulations on the upscaled surface can be compared to simulations with the resolved surface to determine the reliability of the upscaling approach. Finally, we assess the relative importance of structural heterogeneity compared to a capillary fringe, another relevant process, through flow simulation on the resolved surface.

4.1. Description of caprock

Two heterogeneous caprock surfaces were compared, each based on datasets developed for the IGeMS project (http://www.nr.no/IGEMS). These large-scale synthetic surfaces (30

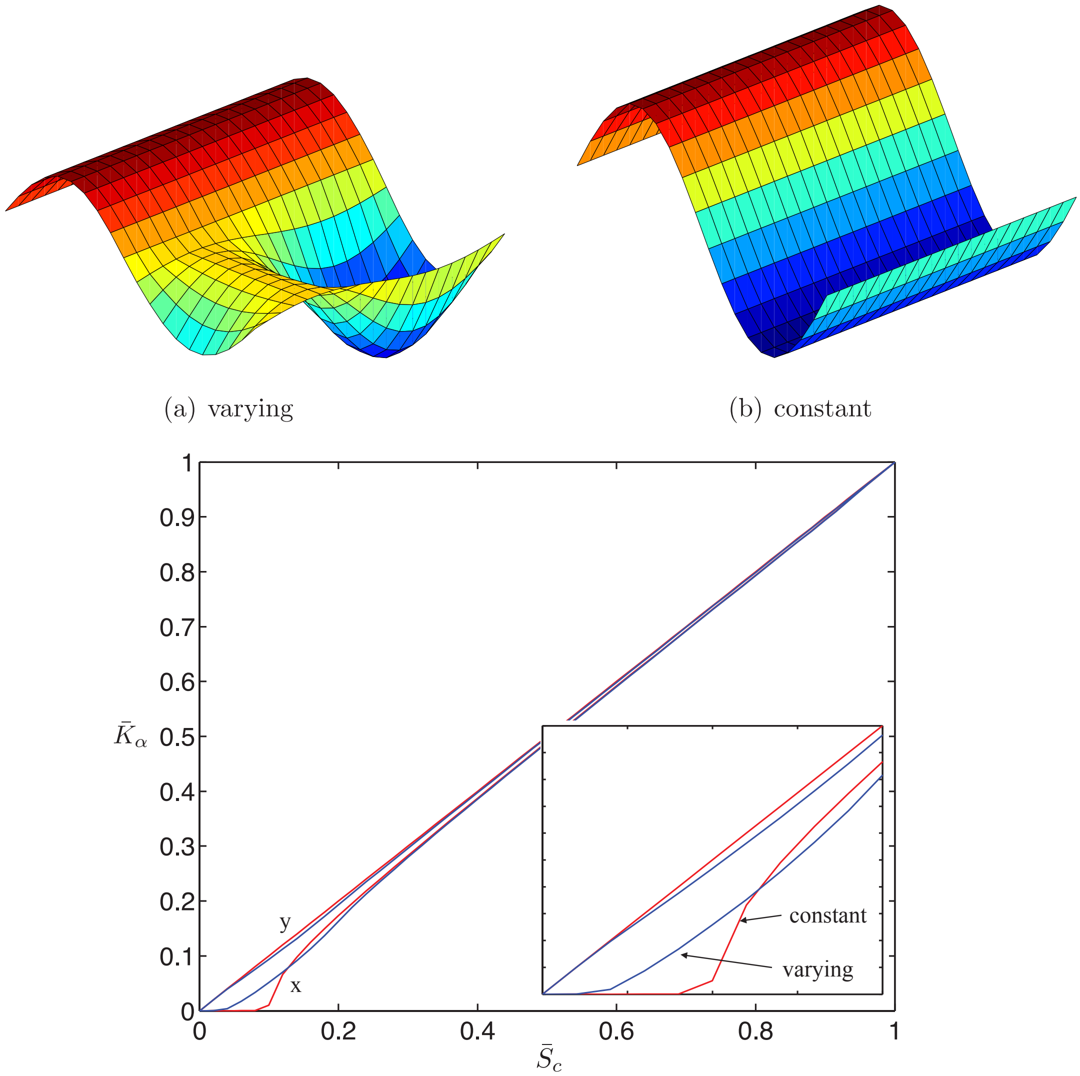

Figure 6: The upper row shows the test case surfaces–the left is a varying spillpoint case while the right can be seen as a constant case. The lower panel shows the relative permeability of CO_2 for the two surfaces in both the x and y directions (the inset focuses on the CO_2 curve at low CO_2 saturation). The red line is the constant case and the blue line is the varying case.

Table 2: Heterogeneous parameters for the OSS and FMM caprock surfaces.

Parameter	OSS	FMM
Amplitude	<20m	1–10 m
Width	2–4 km	10–300 m
Spacing	2–4 km	40–300 m
Total Trapped Volume	0.26 km^3	0.85 km^3

× 60 km) were created to represent realistic sandstone storage formations underneath an impermeable caprock that has a shallow 1% dip in one direction. The geological features of the caprock surfaces modeled here are based on the buried offshore sand ridges (OSS) and buried beach ridges in a flooded marginal marine setting (FMM). Although many realizations of each geologic setting were created in the original IGeMS study, only one realization of each of the OSS and FMM surfaces were used in this paper. More details can be found in [22] and the original datasets are available online at the project website. A flat caprock surface with the same large-scale attributes as the heterogeneous surfaces (domain size and tilt) was also tested as a reference for comparison.

The OSS surface consists of relatively large, kilometer-scale structures that are spaced a few kilometers apart. In contrast, the FFM surface has much narrower meter-scale structures that are spaced close together. In both cases, the elliptical structures are oriented perpendicular to the dip direction. The orientation is dependent on the geologic uplift in relation to the depositional environment, and therefore a parallel orientation is equally possible. However, we chose the perpendicular orientation because it produces the maximum trapping potential, which is particularly relevant for the OSS case. Based on the analysis in the previous section, relevant parameters are listed in Table 2.

A series of resolved simulations were performed with the two heterogeneous surfaces and a flat surface. The grid resolution is varied throughout the domain such that the finest resolution of 100 m x 100 m occurs within the region where CO_2 is flowing, with coarser resolution towards the lateral boundaries ($y = 0$ km and $y = 30$ km). CO_2 was injected at a rate of 4 Mt/yr for 50 years through a well located at $x = 15$ km and $y = 15$ km. The first

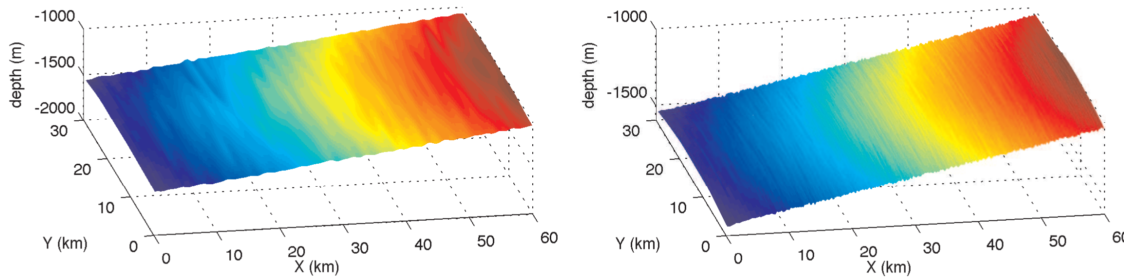

(a) OSS (b) FMM

Figure 7: Heterogeneous caprock surfaces for a tilting saline aquifer (1%) created under two different depositional scenarios: buried offshore sand ridges (OSS) on left, and flooded marginal marine (FMM) on right.

set of simulations assumed a sharp interface (SI), representing an aquifer where the capillary fringe is small compared to aquifer thickness and can be neglected. Additional simulations were performed with a relatively large capillary fringe (CF) to explore the parameter space. All simulations allowed for dissolution due to equilibrium partitioning in residual brine and brine in contact with residual CO_2 but no dissolution due to convective mixing ($C_{\text{diss}} = 0$). The capillary-saturation function employed here is a standard Brooks-Corey function with exponent $m = -1/2$ and coefficient P_0. The relative permeability function is also Brooks-Corey with exponent $n = 3$. A summary of the parameters can be found in Table 3.

Summarizing the resolved simulation results, we see the impact of topography on the plume migration and the distribution of trapped mass Figures 8 and 9. The OSS surface large individual traps collect significant amounts of CO_2, but spread over a greater area than in the FMM case. The capillary fringe also impacts the speed of the plume since the leading edge of the plume is comprised predominantly of low CO_2 saturations that lead to a lower average relative permeability than the SI case. It should be noted that the CF simulations result in less CO_2 stored in each of the structural traps because the capillary fringe leads to a lower average saturation for a given CO_2 plume thickness, defined as the bottom of the mobile CO_2 region ζ_M, particularly at small CO_2 plume thickness values.

Table 3: VE model parameters for heterogenous surface simulations.

Parameter	Value	Unit
Permeability	1	Darcy
Porosity	26	%
Aquifer tilt	1	%
CO_2 density	700	kg/m^3
CO_2 viscosity	0.06	mPa-s
CO_2 residual saturation	0.21	–
CO_2 endpoint permeability	0.75	–
CO_2 solubility	0.02	% mass
Brine density	1020	kg/m^3
Brine viscosity	0.69	mPa-s
Brine residual saturation	0.11	–
Brine endpoint permeability	0.54	–
Brine solubility	0	% mass
Capillary coefficient, P_0	0 (SI)/0.2 (CF)	bar

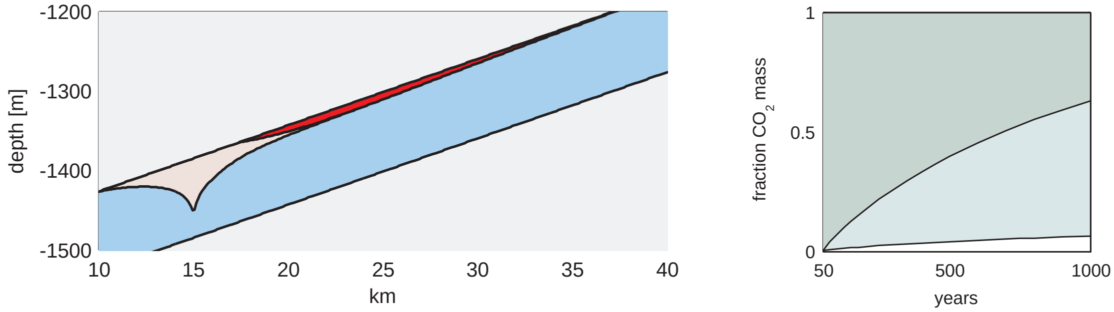

(a) flat

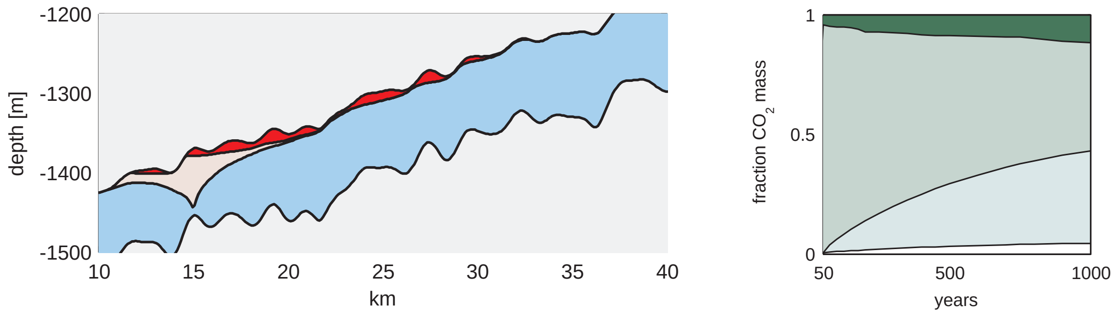

(b) OSS

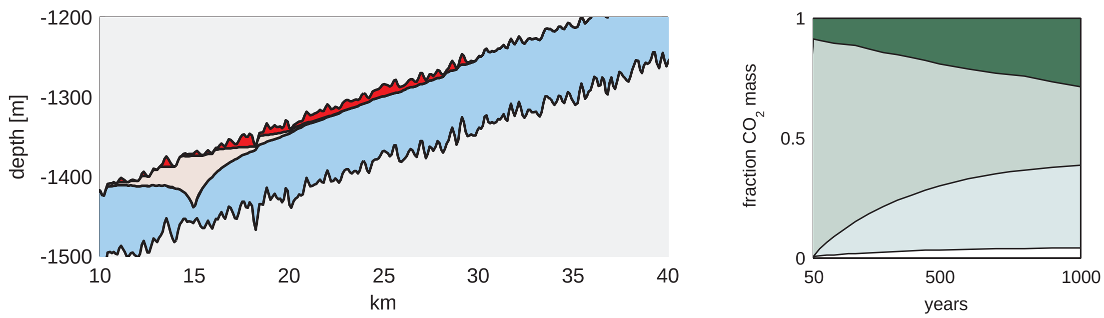

(c) FMM

Figure 8: Results from the sharp-interface resolved simulations (SI) depicted along cross-sections (at y =15km) of the flat (top), OSS (middle), and FMM (bottom) aquifer models. Dark red shaded area is mobile CO_2 region and light red shaded area is region with residually trapped CO_2. Right panels show temporal evolution of distributed CO_2 mass (fraction of total injected) over 1000 years. From top to bottom (dark to light) are structurally trapped CO_2, free CO_2 phase, residual CO_2, and dissolved CO_2.

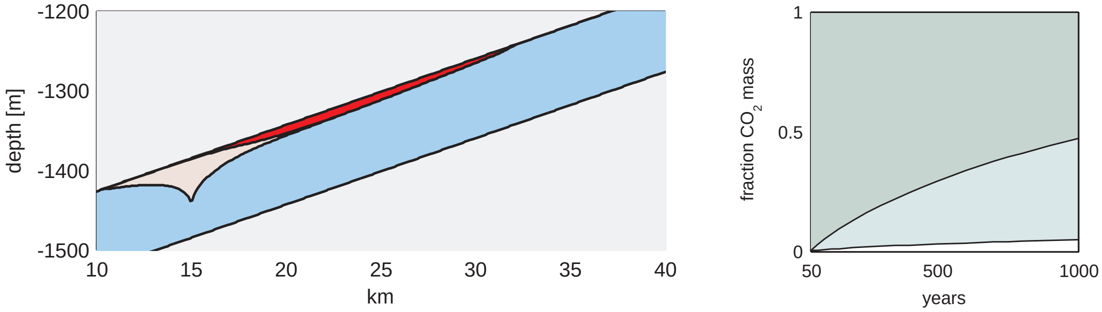

(a) flat

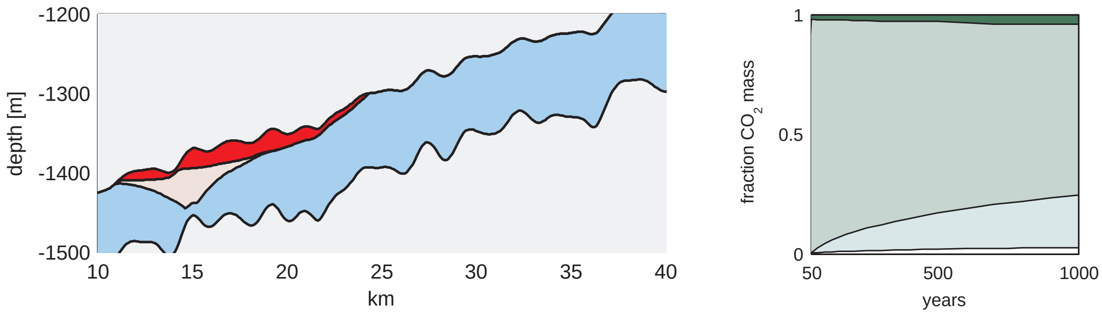

(b) OSS

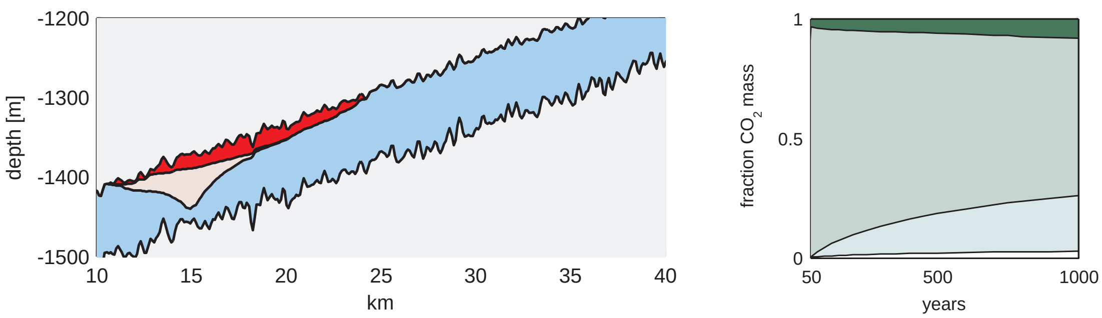

(c) FMM

Figure 9: Results from resolved simulations with capillary fringe (CF) depicted along cross-sections (at y =15km) of the flat (top), OSS (middle), and FMM (bottom) aquifer models. Dark red shaded area is mobile CO_2 region and light red shaded area is region with residually trapped CO_2. Right panels show temporal evolution of distributed CO_2 mass (fraction of total injected) over 1000 years. From top to bottom (dark to light) are structurally trapped CO_2, free CO_2 phase, residual CO_2, and dissolved CO_2.

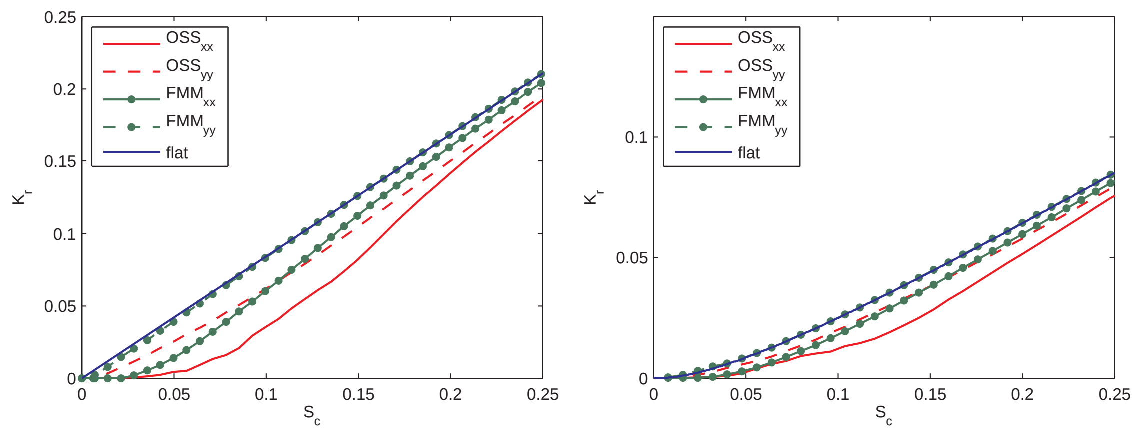

(a) SI (b) CF

Figure 10: Upscaled CO_2 relative permeability curves for the SI (left) and CF (right) fluid properties on the OSS and FMM surfaces, compared with the flat caprock curves for both SI and CF fluid properties.

4.2. Upscaling

The heterogeneous surfaces were upscaled using numerical flow-based upscaling to determine $\bar{\mathbf{K}}_c$ as a function of $\bar{S}_c$ using Equation (8). The steady-state simulations were performed on a subsection equal to one-third of the domain for of each surface, which was done in order to capture several wavelengths of the structures. The CO_2 relative permeability was upscaled for both the sharp interface (SI) and capillary fringe (CF) cases, which are shown in Figure 10. The brine relative permeability is assumed to be unchanged from the vertically upscaled function such that $\bar{\mathbf{K}}_b = \mathbf{K}_b$.

Due to the asymmetric nature of the FMM and OSS surfaces, the upscaling results in tensorial relative permeability for both cases. The xx component is more significantly changed from the reference surface, which is due to the long dimension of the structures being oriented perpendicular to the x direction in both cases. The grid is aligned to the structures, so therefore the off-diagonal component is negligible compared to the others. The OSS structure leads to a more gradual increasing of CO_2 relative permeability with $\bar{S}_c$ than the FMM case, with smaller $\bar{\mathbf{K}}_c$ for all values of $\bar{S}_c$ <0.25. This shows the OSS traps impact the flow of CO_2 much more after the structural residual saturation has been exceeded than the FMM surface.

To perform upscaled simulations of the SI and CF cases, the upscaled relative permeability functions in Figure 10 were employed uniformly in an "effective aquifer"–defined as having a flat caprock surface and constant 100-m thickness. The grid resolution was increased to 400 m, which was uniform across the domain. The resulting plume migration after 600 years shows good comparison to a varying degree with the resolved simulations (plan view in Figure 11). For the SI simulations, the OSS upscaled model underestimates the updip extent of the plume, while the FMM upscaled results give a better comparison. For the CF cases, the OSS upscaled model compares better to the resolved simulations than the FMM, which overestimates plume speed in this case. The better comparison in the CF simulations implies that a capillary fringe has more impact than the OSS and FMM structural effects. Despite the discrepancies seen in Figure 11, the upscaled simulations result in a better representation of plume migration than the reference flat caprock simulations performed with no upscaling (top panels).

As expected, the upscaled models are not able to capture the local distribution of trapped CO_2 over the caprock surface. However, the upscaling is able to capture the large-scale features of the plume to different degrees. The OSS case, which consists of large traps at a similar length scale to the CO_2 plume, leads to a larger discrepancy between the upscaled and resolved simulations. The updip extent of the plume is much smaller, though the lateral width of the plume is similar. The difference occurs because the relative permeability functions are upscaled over a large portion of the OSS surface, assuming the impact of the structures is "homogeneous" over the entire surface. However, it is clear in the resolved simulations that the impact of structures is more heterogeneously, or sparsely, distributed as CO_2 migrates along the surface. The FMM case, with much smaller width traps than the plume has greater homogeneity compared to the scale of the plume, thus the impact is captured better in the upscaled relative permeability functions and results therefore in a more consistent match with the resolved simulations. However, we find that the upscaled models capture the integrated amount of trapped CO_2 over the whole domain reasonably well, as shown in the top panels of Figure 12.

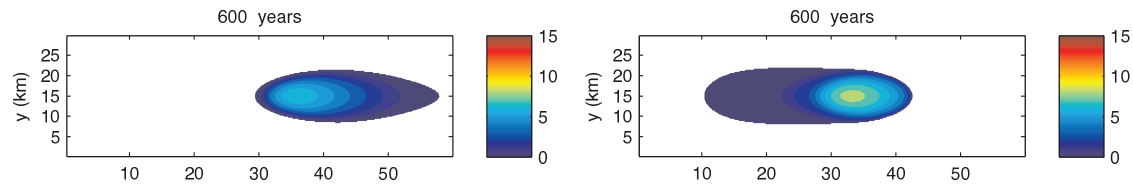

(a) FLAT

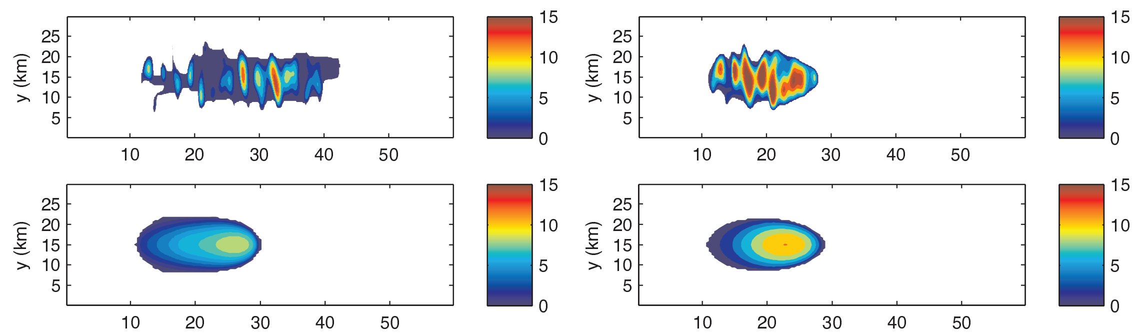

(b) OSS

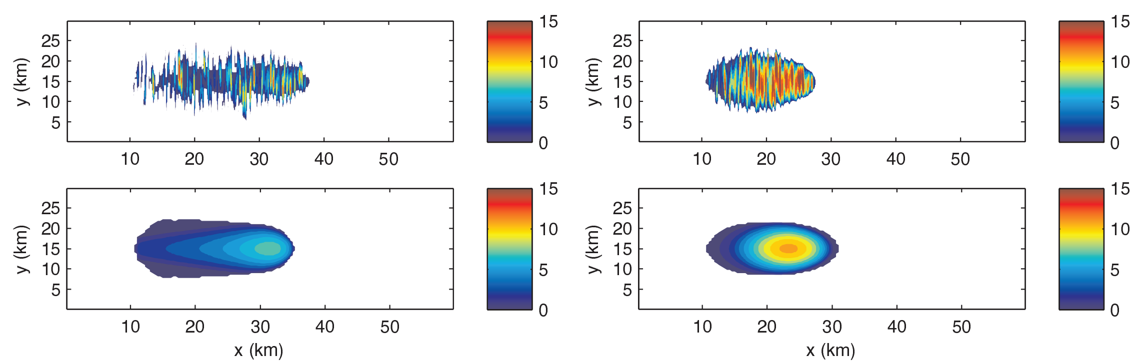

(c) FMM

Figure 11: Comparison of upscaled to the resolved simulations depicting the distribution of CO_2 phase thickness (meters) along the top surface of the domain. SI simulations are shown left and CF simulations are shown right.

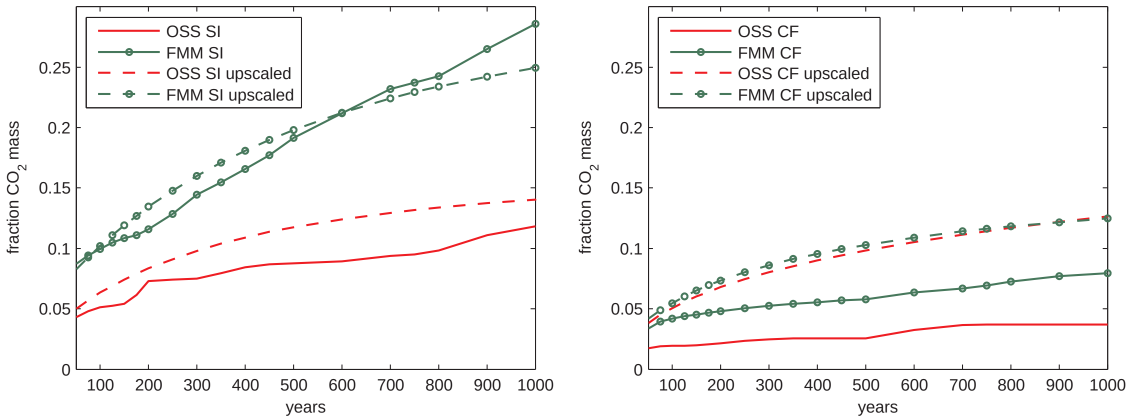

(a) structurally trapped CO_2

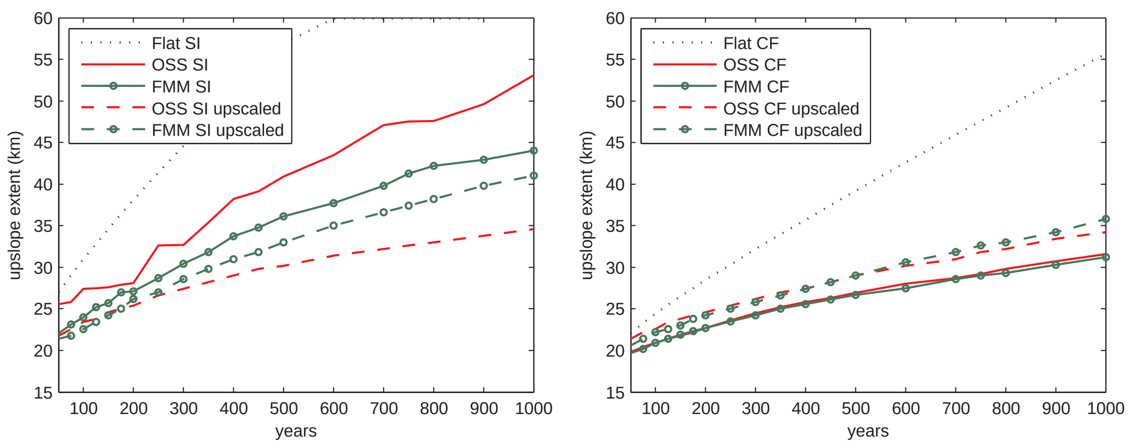

(b) maximum upslope plume extent

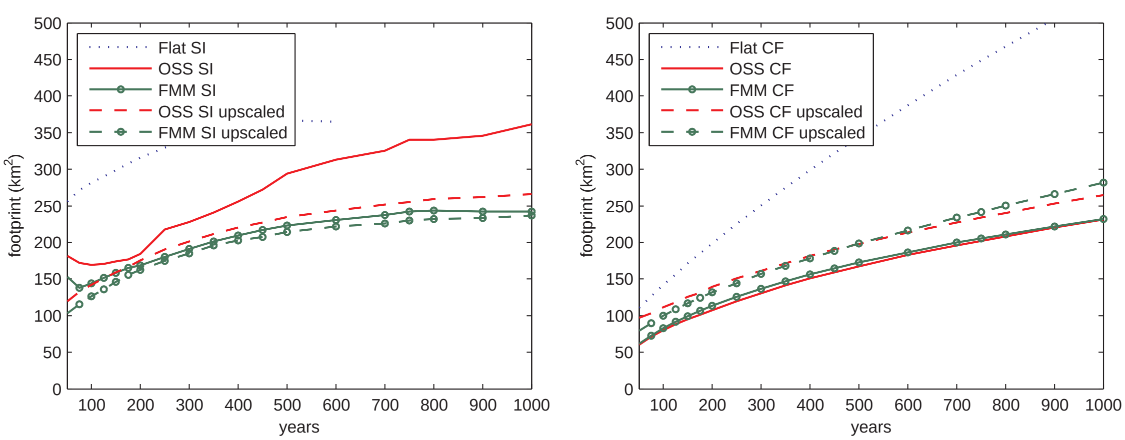

(c) plume footprint size

Figure 12: Comparison of resolved and upscaled simulations on OSS and FMM surfaces. Shown are results for structurally trapped fraction of CO_2 (a), upslope plume extent (b), and plume footprint size (c) for the SI (left) and CF (right) simulations. The upscaled simulations on the OSS and FMM surfaces are compared with the resolved cases and a flat surface where appropriate.

Also in Figure 12, we find the upscaled models have mixed results when comparing upslope extent and plume footprint over the simulated period. In the SI cases, the FMM upscaled simulations are able to capture the impact of topography most effectively, especially with regard to plume footprint. On the other hand, the OSS is unable to capture plume dynamics with much accuracy. The CF simulations had better comparisons overall between the upscaled and resolved cases, with some persistent overestimation. Despite this discrepancy, the rate of increase at late time is nearly the same as the resolved CF simulations.

5. Dimensionless groupings

In this paper we have identified several important topographical parameters that impact upscaled models of CO_2 migration and trapping in structurally heterogeneous systems. First, we investigated idealized topographies to gain insight into the effect of heterogeneity on upscaled relative permeability functions. This analysis leads to simple dimensionless groupings that can be used to estimate the impact of structural heterogeneity that can be expected for different surfaces. The five groupings are summarized in Table 4, which include three new groupings proposed here along with the a and f_c groupings proposed previously [16, 23]. Also included in the table are groupings that compare another important physical process, the capillary fringe, to the influence of structure. These will be discussed further here.

The first key topographical parameter identified in previous work is trapped volume, described by the amplitude ratio a. A larger amplitude ratio means more trapping and a slower migration speed. While amplitude is important, it only determines the structural residual saturation that must be exceeded for CO_2 to flow freely across the surface. Once CO_2 is flowing, the shape of the upscaled relative permeability curve is determined by other structural characteristics that contribute to surface roughness. We identified three dimensionless groups that determine roughness–the relief, tilt and spillpoint ratios–which lead to different impacts on the relative permeability curve.

The relief ratio (f_r) compares the distances between traps to their width for a fixed trapped volume. As the distance decreases from one trap to another, the width of the traps increases in proportion and f_r decreases, thereby increasing roughness. This means that

Table 4: Characteristic groupings of geological and fluid parameters that impact plume migration and trapping along a rough caprock surface. The groupings are quantified for the OSS and FMM surfaces given the parameters listed in Tables 2 and 3

Topography Characteristics	Grouping	OSS	FMM
Amplitude Ratio	$a = \dfrac{A}{\bar{H}}$	0.2	0.1
Relief Ratio	$f_r = \dfrac{l_1}{l_1 + l_2}$	0.5	0.8
Tilt-Wavelength Ratio	$f_t = \dfrac{\lambda}{A} \tan\theta$	1	0.04
Spillpoint Ratio	$f_s = \dfrac{\max \zeta_T}{\min \zeta_T}$	1.5	1
Capillary Ratio	$f_c = \dfrac{p_c'^*}{a\bar{H}\Delta\rho g \cos\theta}$	1.42	2.8

comparing two systems that have the same overall trapping capacity, the one with low-relief, wider features that blend together will have a greater reduction on plume migration speed than a system with more pronounced high-relief features spaced far apart.

The tilt-wavelength ratio (f_t) relates wavelength (λ) to the dip angle (θ) of the aquifer. This ratio can be used to compare the roughness of two surfaces with identical trapping capacity and dip angle, where a lower f_t indicates a lower roughness. The topography with a smallest dominant wavelength results in the smallest roughness because the curvature of the CO_2 relative permeability function is decreased at low wavelength. A reduced curvature implies higher upscaled CO_2 relative permeability for the same plume thickness. The roughness also differs between two surfaces with the same wavelength but a different tilt angle. In this case, the increased tilt angle increases roughness while also decreasing the trapping capacity of the surface. And finally, the tilt-wavelength ratio indicates that two horizontal surfaces ($\theta = 0$), which only differ in wavelength, will have the same relative permeability functions.

The fourth grouping, spillpoint ratio (f_s), compares the distribution of spillpoint depths over the averaging area and can only be identified for two-dimensional surfaces. A large ratio means the difference between the shallowest and deepest spillpoint is large and the roughness of the surface is greater. The roughness is increased because although CO_2 flow is initiated over the shallow spillpoints early, the transition to a fully flowing CO_2 plume (reaching beyond the deepest spillpoint) is slow. Therefore, the caprock continues to impact plume speed even for a smaller trapped volume overall. This affects the upscaled relative permeability function by creating a smoother transition from non-flowing to the flowing regime compared to a case with all spillpoints at the same level. Different spillpoint distributions will lead to different flow regimes and corresponding upscaled relative permeability curves.

Given this set of structural parameter groupings, it is necessary to evaluate their utility for understanding CO_2 migration along more realistic heterogeneous surfaces. To do this, simulations were performed along two surfaces, OSS and FMM, that were inspired by different depositional settings common in sedimentary basins. We can compare the quantified dimensionless groupings for each surface (given in Table 4) with the respective upscaled relative permeability curves and simulation results. It should be noted that there are several impacts occurring simultaneously, so making exact comparisons with dimensionless groupings is difficult. Regardless, some interesting observations can be made.

In the upscaled relative permeability functions seen in Figure 10, the OSS curve indicated a rougher surface with little trapping. The quantified values in Table 4 show that the OSS surface has a higher amplitude ratio, which would normally indicate a larger structural residual saturation than the FMM curve. However, the total trapped volume for the OSS over the entire surface is lower than the FMM (Table 2), leading to flow starting at a lower average CO_2 saturation than the FMM curves.

This discrepancy indicates that some other structural factors are dominant. For example, the FMM relief ratio is higher than the OSS, indicating that the OSS is rougher, but the values do not differ greatly. A similar conclusion can be drawn from a comparison of f_s. On the other hand, the value of f_t for OSS is nearly two orders of magnitude greater than the FMM. This is because the geologic parameters (width and spacing) given for the OSS in Table 2 result in kilometer-scale wavelength compared with 100 meters for the FMM. Therefore, we conclude that the moderate tilt combined with a long wavelength has the most significant impact on the increased curvature of OSS relative permeability curves compared to the FMM. The larger OSS wavelength can also explain a decreased trapping (because of the tilted surface) despite having a larger amplitude.

The flow simulations on the OSS and FMM surfaces are also valuable for comparing the relative importance of structural effects to other processes that impact CO_2 flow over large scales. For example, in Section 4, we performed simulations with a relatively large capillary fringe. Similar to previous work [23], we observed that a capillary fringe also slows the plume migration, and becomes important as the length scale of the fringe increases compared with the vertical dimension of the aquifer. The fringe also competes with structural roughness in slowing the plume migration, i.e. the relative impact of the structural effects increases as the capillary length scale decreases and vice versa. The capillary fringe ratio f_c gives an indication of the relative strength of these effects. As the capillary ratio decreases, the structures dominate the flow. Conversely, capillarity will dominate if the fringe is much larger than the dominant amplitude of the structures. We see that the OSS has the smaller capillary ratio, but the upscaled relative permeability curves and simulation results indicate that a sufficiently large capillary fringe will overwhelm the structural heterogeneity for both the OSS and FMM caprock surfaces.

6. Upscaling considerations

This study gives valuable insight into the effectiveness of upscaled models under realistic geological settings and fluid properties. By comparing the length scale of the plume to that of the main structures, we can evaluate the conditions under which upscaling is a practical means of simplifying the system while still capturing the CO_2 plume dynamics and trapping.

For example, we observed that the upscaled OSS model performed poorly for all aspects of the SI simulation, the scenario for which structural effects are most important. The relatively poor representation of the resolved model occurred because the upscaled functions were employed in grid blocks whose size was much smaller (400 m) than the width of the structural features (2000 m). This led to trapping of CO_2 that was correct on average, but did not capture the large-scale distribution of trapped CO_2 as compared with the resolved model. Also, plume migration speed was impacted homogeneously over the entire upscaled surface, even though the traps were more sparsely spaced.

We should expect that the upscaled model will not perform well when the width of the dominant structural features is significantly larger than the model resolution scale. It should be noted that the scale separation needed for flow-based upscaling is not strictly fulfilled for the example surfaces. This is true even for the FMM case that consists of smaller wavelength structures, despite our finding that the upscaling works relatively well in that case. Our methodology would be better for upscaling sub-grid effects, i.e. only the wavelengths shorter than the 400 m grid resolution used in upscaled simulations. However, our aim was to see if upscaling the larger wavelengths could be applied for the given examples. Ultimately, the upscaling is better suited for much larger storage systems, such as the large-scale aquifers in the North Sea [24], where the subscale wavelengths are known and can be upscaled in a step-wise manner for each coarsened gridblock.

An alternative to upscaling is to simply coarsen the domain without employing upscaled relative permeabilities. In the OSS case, grid coarsening without upscaling would likely produce a sufficiently accurate solution. This has been demonstrated in previous work [9], which shows that coarsening the grid from 100 m to 400 m still provides sufficient resolution for the OSS case. If the surface is such that grid coarsening is inaccurate, it is also possible to consider a different approach to upscaling only the smaller wavelength features of the surface. In the FMM case, upscaling seems to be a sufficient approach since the width of the features is generally smaller than the upscaled grid block. Grid coarsening would be inappropriate for the FMM and lead to smoothing of the small features and underestimation of the topographical impact [9].

7. Summary and Conclusions

The key requirement of CO_2 storage simulations is the ability to perform large-scale simulations which describe the main physics of the plume over multiple length and time scales. We have focused on structural heterogeneity and its impact on plume migration and trapping in this paper. This modeling process may require upscaling of fine-scale geological features, for which all the details may not be known or observable. Hence, it is important to determine the detailed information that is necessary to get to correct upscaled behavior. We identified some of the main parameters of the top surface topography which govern the plume migration. In particular, we show how these parameters affect the upscaled relative permeability functions. Subsequently, we discussed the effect of the parameters in the context of full field simulations on two different topographical cases. And finally, we discussed how the effects of the top surface structure interact with the main physical forces in a VE setting, which include surface tilting and strength of capillary forces, for the given cases.

We investigated the use of flow-based upscaling for performing direct numerical simulations and investigating flow characteristics of real field models. The main findings of the paper is a set of parameter groupings, which can be easily found for a surface and give information about trapping volume, sensitivity to tilt angle and flow characteristics of a plume. These parameters are valuable for deciding on a simulation strategy that introduces subscale features into a large-scale simulation. In particular, we have shown that the most important features that must be captured are as follows, with decreasing order of importance:

- amount of trapped CO_2, which impacts the point at which CO_2 begins to flow freely; and
- the features that affect CO_2 flow at the start of the flowing regime.

While the dimensionless groupings are an important result of this work and give insight into how CO_2 flow will be impacted for a given caprock surface, we emphasize that the dimensional analysis should be accompanied by simulation studies on the upscaled model. In addition, the utility of the groupings should be further explored for a greater variety of geologic models.

We have shown that the best approach for long-term storage capacity or storage security simulations can be guided by an evaluation of the dominant structural characteristics. In particular, expensive grid refinement often associated with large-scale simulation can be avoided by the proper choice of upscaling or grid coarsening. These results also give insight into how a complex geological model can be simplified. For example, we have shown that detailed knowledge of the surface is only needed in locations where the plume thickness is small, which will occur mainly near the edges of the migrating plume. Through model simplification using appropriate techniques, large-scale CO_2 simulation can be performed more efficiently and effectively for real storage systems.

8. Acknowledgements

This work was funded by the MatMoRA-II project, Contract no. 21564, sponsored by the Research Council of Norway and Statoil ASA.

References

[1] M. J. Bickle, Geological carbon storage, Nature Geoscience 2 (12) (2009) 815–818.

[2] B. Metz, O. Davidson, H. de Coninck, M. Loos, L. Meyer (Eds.), IPCC special report on carbon dioxide capture and storage, Cambridge University Press, New York, USA, 2005.

[3] W. A. Ambrose, S. Lakshminarasimhan, M. H. Holtz, V. Nunez-Lopez, S. D. Hovorka, I. Duncan, Geologic factors controlling CO_2 storage capacity and permanence: case studies based on experience with heterogeneity in oil and gas reservoirs applied to CO_2 storage, Environmental Geology 54 (8) (2008) 1619–1633.

[4] A. Kopp, H. Class, R. Helmig, Investigations on CO_2 storage capacity in saline aquifers-part 2: Estimation of storage capacity coefficients, International Journal of Greenhouse Gas Control 3 (3) (2009) 277–287.

[5] J. M. Nordbotten, M. A. Celia, Geological Storage of CO_2: Modeling Approaches for Large-Scale Simulation, John Wiley & Sons, Inc., 2012.

[6] C. Hermanrud, T. Andresen, O. Eiken, H. Hansen, A. Janbu, J. Lippard, H. N. Bolås, T. H. Simmenes, G. M. G. Teige, S. Østmo, Storage of CO_2 in saline aquifers-lessons learned from 10 years of injection into the Utsira Formation in the Sleipner area, Energy Procedia 1 (1) (2009) 1997–2004.

[7] G. T. Eigestad, H. K. Dahle, B. Hellevang, F. Riis, W. T. Johansen, E. Øian, Geological modeling and simulation of CO_2 injection in the Johansen formation, Comp. Geosci. 13 (4) (2009) 435–450.

[8] M. Elenius, J. Nordbotten, K. H., Effects of a capillary transition zone on the stability of a diffuse boundary layer, IMA Journal of Applied Mathematics 77 (6) (2012) 771–787.

[9] H. Nilsen, A. R. Syversveen, K.-A. Lie, J. Tveranger, J. M. Nordbotten, Impact of top-surface morphology on CO_2 storage capacity, International Journal of Greenhouse Gas ControlUnder review.

[10] S. E. Gasda, J. M. Nordbotten, M. A. Celia, Application of simplified models to CO_2 migration and immobilization in large-scale geological systems, International Journal of Greenhouse Gas Control 9 (2012) 72–84.

[11] M. A. Hesse, F. M. Orr, H. A. Tchelepi, Gravity currents with residual trapping, Journal of Fluid Mechanics 611 (2008) 35–60.

[12] M. J. Golding, J. A. Neufeld, M. A. Hesse, H. E. Huppert, Two-Phase gravity currents in porous media, Journal of Fluid Mechanics (2011) 1–23.

[13] R. Juanes, C. W. MacMinn, M. L. Szulczewski, The footprint of the CO_2 plume during carbon dioxide storage in saline aquifers: Storage efficiency for capillary trapping at the basin scale, Transport in porous media 82 (1) (2010) 19–30.

[14] J. M. Nordbotten, H. K. Dahle, Impact of the capillary fringe in vertically integrated models for CO_2 storage, Water Resources Research 47 (2011) W02537.

[15] S. E. Gasda, J. M. Nordbotten, M. A. Celia, Vertically-averaged approaches for CO_2 injection with solubility trapping, Water Resources Research 47 (2011) W05528.

[16] S. Gasda, H. Nilsen, H. Dahle, W. Gray, Effective models for CO_2 migration in geological systems with varying topography, Water Resources Research 48 (2012) W10546.

[17] W. G. Gray, P. Herrera, S. E. Gasda, H. K. Dahle, Derivation of vertical equilibrium models for CO_2 migration from pore scale equations, International Journal of Numerical Analysis and Modeling 9 (3) (2012) 745–776.

[18] J. Bear, Dynamics of Fluids in Porous Media, American Elsevier Publication Co., New York, N.Y., 1972.

[19] P. Renard, G. de Marsily, Calculating equivalent permeability: a review, Advances in Water Resources 20 (5–6) (1997) 253–278.

[20] G. Pickup, K. Stephen, An assessment of steady-state scale-up for small-scale geological models, Petroleum Geoscience 6 (3) (2000) 203–210.

[21] I. Neuweiler, H.-J. Vogel, Upscaling for unsaturated flow for non-Gaussian heterogeneous porous media, Water Resources Research 43 (3) (2007) W03443. doi:10.1029/2005WR004771.

[22] A. Syversveen, H. Nilsen, J. T. K.-A. Lie, P. Abrahamsen, A study on how top-surface morphology influences the CO_2 storage capacity, in: P. Abrahamsen, R. Hauge, O. Kolbjrnsen (Eds.), Geostatistics Oslo 2012, Vol. 17, 2012, pp. 481–492.

[23] S. Gasda, H. Nilsen, H. Dahle, Effective models for CO_2 migration in geological systems with varying topography, in: Proceedings of XIX International Conference on Computational Methods in Water Resources, 17-22 June 2012, University of Illinois at Urbana-Champaign, USA, 2012.

[24] Norwegian Petroleum Directorate, CO_2 Storage Atlas: Norwegian North Sea, Stavanger, Norway, 2011.